Pixel-scale composite top-of-the-atmosphere clear-sky reflectances for Meteosat-7 visible data

A. Ipe, N. Clerbaux, C. Bertrand, S. Dewitte, and L. Gonzalez

Section Remote Sensing from Space, Department of Observations, Royal Meteorological Institute of Belgium, Brussels, Belgium

[1]   A new method to estimate composite top of the atmosphere (TOA) visible clear-sky reflectances for wide narrow band geostationary satellites such as the Meteosat constellation is presented. This method relies on some a priori knowledge of angular variations of TOA broadband reflectances associated with clear-sky conditions above mean surface types through the use of the clear-sky Cloud and the Earth's Radiant Energy System (CERES) shortwave broadband angular dependency models (ADMs). Each pixel (or Earth location) viewed from such geostationary imager at a given daytime is associated with a reflectance time series made up of its chronological daily measurements. This time series can be seen as a clear-sky visible narrow band reflectance curve of the associated pixel surface plus an additive random noise modeling cloudy conditions above it. On the basis of this assumption, TOA clear-sky broadband reflectances extracted from the CERES ADMs are used to compute curve-driven fifth percentiles on these time series in order to estimate the TOA clear-sky visible narrow band reflectance curves for all pixels, while the percentile approach exhibits only a reduced sensitivity to cloud shadows. Benefits of our method are discussed with respect to its application to 7 months of Meteosat-7 daytime visible narrow band measurements. Finally, the performance of our algorithm is assessed through comparisons with its predicted and associated International Cloud Climatology Project DX clear-sky values with respect to a visually generated clear-sky pixels database.   *INDEX TERMS:* 3359 Meteorology and Atmospheric Dynamics: Radiative processes; 3360 Meteorology and Atmospheric Dynamics: Remote sensing; 3394 Meteorology and Atmospheric Dynamics: Instruments and techniques; *KEYWORDS:* pixel-scale, TOA composite, clear-sky, Meteosat-7 imager

1. Introduction

[2] Inference of the top of the atmosphere (TOA) visible clear-sky reflectances from satellite narrow band imagers is crucial in remote sensing. Such a scheme is the first step of nearly all cloud algorithms which aim to retrieve cloud parameters (see *Rossow et al.* [1989] for a nonexhaustive historical survey of cloud algorithms) in order to study, for example, cloud radiative feedbacks. The TOA visible clear-sky reflectances are usually used by these algorithms to detect the presence of clouds in the observed scenes. Moreover, with the use of radiative transfer models, these TOA visible clear-sky reflectances can be inverted to derive surface properties such as biomass estimation over vegetation through vegetation indices and surface albedos. In addition, a monitoring of these surface properties may also be indicative of climate variations.

[3] A number of algorithms devoted to perform this clear-sky determination can be found in the literature. These are generally based on the common assumptions that (1) clear-sky visible reflectance variations are smaller in time than in space (especially over land), and (2) surface reflectance variations are smaller than variations associated with the cloud reflectances. As an example, *Minnis and Harrison* [1984a] generated composite clear-sky images from the Geostationary Operational Environmental Satellite (GOES) data by applying a minimum reflectance threshold criterion to identify clear scenes as a function of surface type and geographic region. Unfortunately, to avoid cloud contamination, the threshold values have to be extracted from some subsampling of minima values in the reflectance time series with respect to some standard deviation criteria. This therefore requires more information on the reflectance distributions than simply the minimum values. Moreover, as pointed out by *Matthews and Rossow* [1987], such a technique of clear-sky determination is sensitive to the scene geometry variations and to the atmospheric noise

such as cloud shadows. Regarding the International Satellite Cloud Climatology Project (ISCCP), *Rossow and Garder* [1993] developed an algorithm based on a spatial and temporal homogeneity test (as well as several geotypes) to be applied at the regional grid cells. In addition, scene geometry variations are corrected to the first order according to the solar zenith angle. ISCCP also relies on the *Minnis and Harrison* [1984a] empirical bidirectional reflectance model for clear-sky ocean and assumes isotropic clear-sky reflectance over land although it has been established that the anisotropy of the land scenes is significant [*Minnis and Harrison*, 1984b].

[4] Being involved in the Geostationary Earth Radiation Budget (GERB) radiometer ground segment (which aims to deliver near real-time estimates of the TOA radiative broadband fluxes at the high spatial resolution of 10 km at nadir with the help of the Spinning Enhanced Visible and InfraRed Imager (SEVIRI) for the limited geographical area covered by Meteosat Second Generation (MSG) satellite), one of Royal Meteorological Institute of Belgium (RMIB) preoperational activities was to test the RMIB GERB Processing (RGP) on Meteosat-7 (MS-7) data and to derive GERB-like products without any associated broadband radiometer information. Such data after adequate validation with real GERB products will certainly prove to be valuable to the future GERB users by extending back in time the availability of GERB data prior to the routine exploitation of MSG. In order to process MS-7 data by the RGP as suggested, we need to generate clear-sky images for the MS-7 visible narrow band channel at every 30 min sampling daytime. Algorithms as previously developed to deal with the Scanning Radiation Budget (ScaRaB) data [*Stubenrauch et al.*, 2002] and/or the ISCCP data are not suited for GERB data processing since we need to retain the high spatial resolution of MS-7 visible images (2.5 km at nadir). Moreover, the composite clear-sky images as produced by using such algorithms are time-averaged over a couple of hours which is incompatible with the high temporal resolution of MS-7 (30 min) and the geostationary platforms (large variations in the Sun-Earth-satellite viewing geometry).

[5] Our paper aims therefore to present an innovative method which accounts for high Sun-Earth-satellite (or scene) viewing geometry variations (see Figure 1b) and a high spatial resolution of the imager when estimating composite TOA clear-sky visible reflectances from narrow band geostationary satellite measurements. The benefits and simplicity of this new approach are discussed with respect to its application to 7 months of Meteosat-7 daytime visible measurements. In order to assess the performance of this new method compared to region-based algorithms found in the literature, comparisons are performed between those two approaches and a database of MS-7 clear-sky pixels. In the following, visible has to be understood as visible narrow band, and shortwave refers to the spectral interval of 0.3–4.0 μm.

2. Clear-Sky Detection Algorithm

[6] As noted by *Rossow et al.* [1989], grassland and desert surface reflectances can exhibit large spatial variations. Thus, considering each pixel (i.e., fixed location on Earth surface) independently, we only have to deal with a
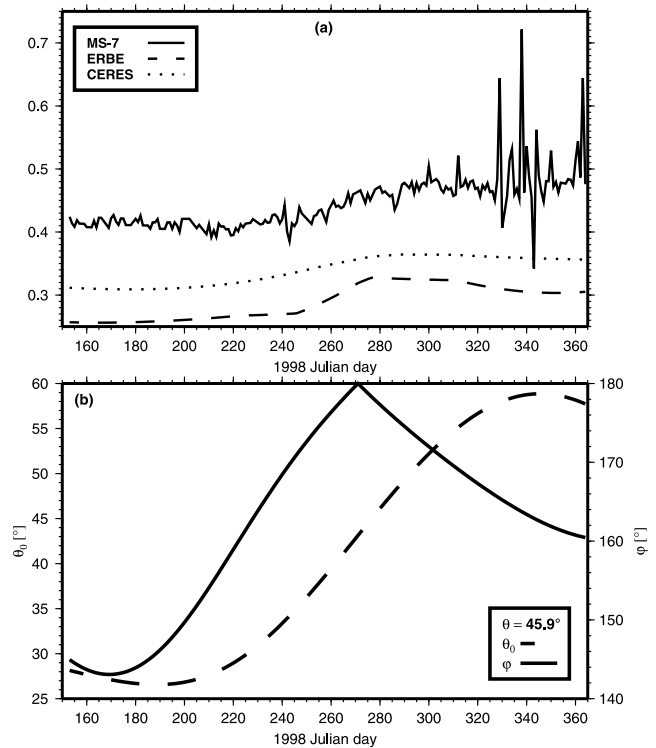

Figure 1. (a) Meteosat-7 visible reflectance time series, ρ_m, and associated clear-sky shortwave ERBE and CERES reflectances, ϱ, according to (b) scene-viewing geometry variations (θ_0 = solar zenith angle, θ = viewing zenith angle, and φ = relative azimuth angle) from the 1200 UTC daily measurements over a bright desert pixel (27.18°N, 30.12°E).

visible reflectance distribution affected by the surface temporal variations, the illumination and the cloudiness. Surface variations are mainly known to occur over vegetated surfaces and are a function of the vegetation age and fractional coverage. According to *Matthews and Rossow* [1987] the seasonal surface reflectance variations over Africa (which is located in the center of the field-of-view (FOV) of MSG) are small because of the presence of large areas of desert and evergreen forests. Therefore, assuming that vegetated surfaces are stable over a restricted time period, the signal measured by the instrument during this period can be considered as only a function of the scene-viewing geometry and cloudiness. For a given daytime hour (i.e., time slot) and a given pixel viewed from a geostationary imager we can associate the visible reflectance time series made up of its chronological daily visible measurements. This time series can then be split into two components: (1) a base curve representative of the clear-sky conditions, and (2) a noise component representing the clouds contributions above the ground surface associated to the pixel. Note that for areas with broken clouds, an additional effect has to be taken into account: The cloud shadows on neighboring pixels decrease the reflectance below the expected clear-sky value. Such an effect is well highlighted in Figure 1 where the sudden and abrupt decrease of the reflectance value measured on day 343 in regard to the other displayed MS-7 reflectances can easily
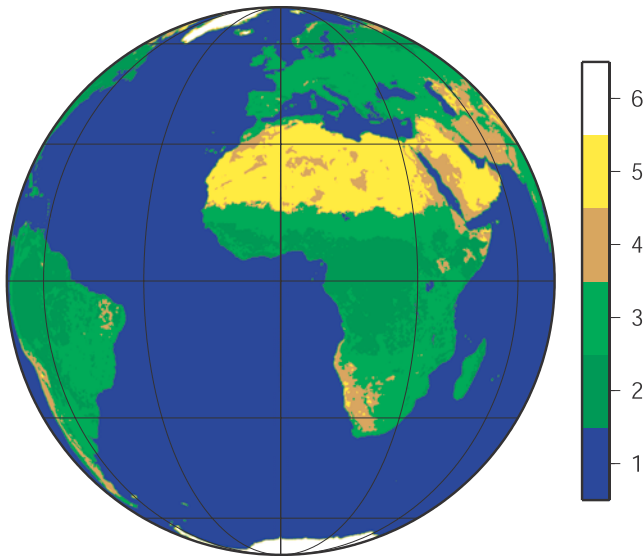
Figure 2. CERES ADMs surface geotypes as seen by Meteosat-7 imagers (1 is ocean, 2 is moderate-to-high vegetation cover, 3 is low-to-moderate vegetation cover, 4 is dark desert, 5 is bright desert, and 6 is snow or ice) [*Loeb et al.*, 2003]. ERBE ADMs surface classification is obtained by grouping dark and bright deserts in one desert class and low-to-moderate and moderate-to-high vegetation covers in one land class.

be explained by the neighboring pixels cloud shadow contamination.

[7] MS-7 visible narrow band images have been used to illustrate the performance of our algorithm, but this technique is obviously applicable to any geostationary imager with a similar wide visible channel. Registered visible MS-7 count images (coded on 8 bits) were retrieved from the Meteosat Archive and Retrieval Facility (MARF) in 5000 × 5000 pixels. These count values were then converted into reflectances with the help of the European Organisation for the Exploitation of Meteorological Satellites (EUMETSAT) time-dependent count-to-radiance calibration scheme from *Govaerts et al.* [2001]. This scheme provides coefficients that are linearly and continuously varying with time; thus it is not expected any discontinuity in the measured reflectances due to updated calibration information as could be the case for other imagers.

[8] Here we propose to use the clear-sky Cloud and the Earth's Radiant Energy System (CERES) shortwave broadband ADMs [*Loeb et al.*, 2003] and their associated geotype classification (see Figure 2) to extract the visible clear-sky base curve from the MS-7 signal. ADMs used in this paper follow the definition from *Taylor and Stowe* [1984]. They are built for some scene stratifications (surface geotypes, cloud fractional covers, cloud phase and cloud optical depth for CERES, coarser surface geotypes, and cloud fractional covers for Earth Radiation Budget Experiment (ERBE)) and some angular bins for scene-viewing geometry (see Table 1). Basically, an ADM is constituted by an anisotropic function R

$$R(\theta_0, \theta, \varphi) = \frac{\pi L^\uparrow(\theta_0, \theta, \varphi)}{F^\uparrow(\theta_0)} \qquad (1)$$

and a broadband albedo A

$$A(\theta_0) = \frac{F^\uparrow(\theta_0)}{E_0 \cos \theta_0} \qquad (2)$$

where, θ_0, is the solar zenith angle, θ, is the viewing zenith angle, φ, is the azimuth angle relative to the solar plane ($\varphi = 0$ corresponds to forward scattering), $L^\uparrow$, is the mean TOA outgoing broadband radiance for given scene type [W m^{-2} sr^{-1}], $F^\uparrow$, is the mean TOA outgoing broadband flux for given scene type [W m^{-2}] and E_0, is the solar constant corrected for Sun-Earth distance [W m^{-2}]. By multiplying equations (1) and (2), we obtain

$$R(\theta_0, \theta, \varphi) \cdot A(\theta_0) = \frac{\pi L^\uparrow(\theta_0, \theta, \varphi)}{E_0 \cos \theta_0} = \varrho(\theta_0, \theta, \varphi)$$

where ϱ is the TOA shortwave bidirectional reflectance distribution function (BRDF) for the associated mean scene type. Thus clear-sky ADMs allow us to compute mean TOA shortwave BRDFs associated with some surface types under clear-sky conditions.

[9] While ERBE and CERES ADMs are built from shortwave measurements, they provide some qualitative knowledge on angular variations of TOA visible BRDFs for associated surfaces. This is illustrated in Figures 1a and 1b, where we plotted TOA Meteosat-7 visible reflectance and ERBE and CERES clear-sky shortwave reflectance time series for a given pixel and its associated scene-viewing geometry variations. We can observe that ERBE and CERES curves have shapes similar to the clear-sky visible reflectance base curve that we want to estimate, although they are offset from each other. As shown in Figure 1a, the use of CERES ADMs leads to a TOA broadband reflectance time series,

Table 1. ERBE and CERES ADM Angular Bin Definitions[a]

Solar Zenith Angle θ_0	Viewing Zenith Angle θ	Relative Azimuth φ
	ERBE[b]	
0−26	0−15	0−9
26−37	15−27	9−30
37−46	27−39	30−60
46−53	39−51	60−90
53−60	51−63	90−120
60−66	63−75	120−150
66−73	75−90	150−171
73−78		171−180
78−84		
84−90		
	CERES[c]	
0−10	0−10	0−10
10−20	10−20	10−30
20−30	20−30	30−50
30−40	30−40	50−70
40−50	40−50	70−90
50−60	50−60	90−110
60−70	60−70	110−130
70−80	70−80	130−150
80−90	80−90	150−170
		170−180

[a]Values are given in degrees.
[b]Source is *Suttles et al.* [1988].
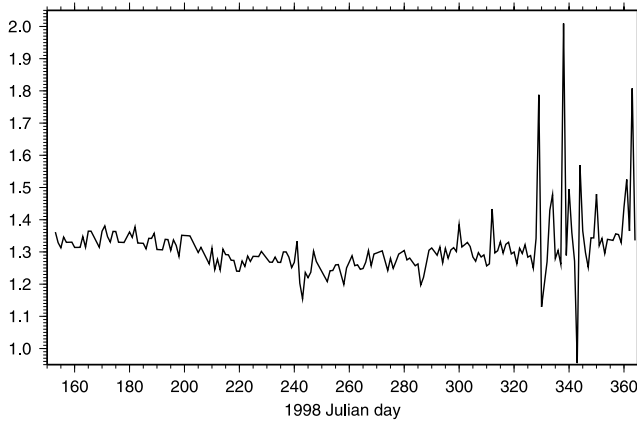[c]Source is *Loeb et al.* [2003].

Figure 3. Ratio of the Meteosat-7 visible reflectances, ρ_m, and associated clear-sky shortwave CERES reflectances, ϱ_c, for the same pixel as in Figure 1.

which is less broken than when using ERBE ADMs because of their coarser angular resolution. The offset between the CERES and ERBE curves can be explained from differences in surface type classification and in clear-sky conditions (cloud fractional cover up to 5% for ERBE and 0.1% for CERES) for the ADMs. By contrast, the offset between Meteosat-7 and these shortwave reflectance curves are due to the fact that the ADMs were built from shortwave measurements and global averaging of each geotype's responses. For a given day ($d^\star$ = current Julian day) and time slot ($t^\star$ = hour) we build the composite TOA visible clear-sky image ρ_{cs} by using for each pixel the following formulation:

$$\rho_{cs}(x, y, d^\star, t^\star) = \alpha(x, y, d^\star, t^\star, N) \cdot \varrho_c(x, y, d^\star, t^\star)$$

where x and y are the pixel coordinates in images and α is a multiplicative factor determined for a given time period of N days. This factor is used to shift the shortwave CERES reflectance curve, ϱ_c, in such a way that only 5% of the measured visible reflectances over the given time period, ρ_m, are kept below the CERES curve. This can be seen as a
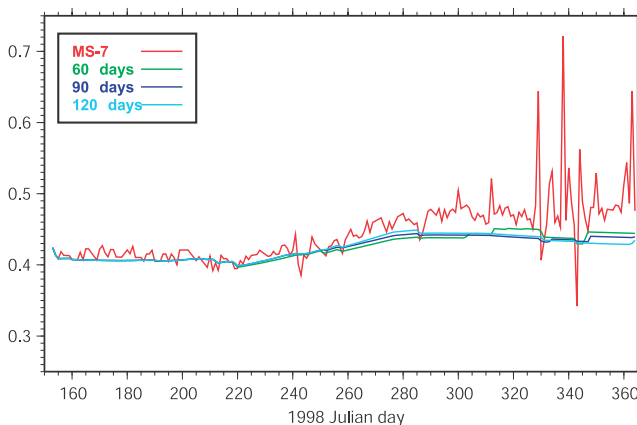

Figure 4. Reflectance time series, ρ_m, of the same Meteosat-7 pixel as in Figure 1 and TOA visible clear-sky values, ρ_{cs}, for several N as predicted by our algorithm.
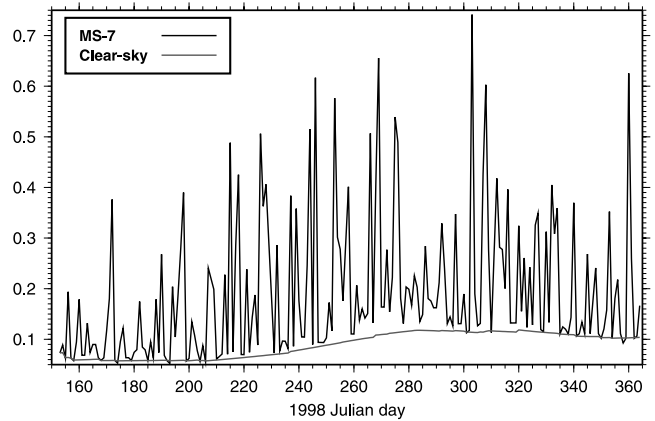

Figure 5. Meteosat-7 visible reflectance time series, ρ_m, and TOA visible clear-sky values, ρ_{cs}, as predicted by our algorithm (N = 60 days) from the 1200 UTC daily measurements over an ocean pixel (4.42°S, 1.28°E).

curve-driven fifth percentile search which reduces to estimate

$$\alpha(d^\star, t^\star, N) = \text{5th percentile of } \frac{\rho_m(d, t^\star)}{\varrho_c(d, t^\star)} \text{ for } d = d^\star - N, \ldots, d^\star.$$

(Note that we implicitly assumed the pixel coordinates dependence in our formulation). It must be noted that such a scheme relies on the assumption that clear-sky shortwave CERES BRDF, ϱ_c, curve and clear-sky visible Meteosat-7 base curve, ρ_{cs}, only differ by a constant multiplicative factor over some temporal extend, N, (i.e., some limited range in the scene-viewing geometry). Restating differently the previous assumption, we are supposing that these two curves only differ by their respective albedos, A, and not by their anisotropy functions, R. Note that cruder approximations can be found in the literature. As an example, *Gruber and Winston* [1978] assume equality of narrow band and broadband albedos. *Minnis and Harrison* [1984b] derived regressional equations from coincident measurements of narrow band and broadband reflectances according to scene conditions. However, as suggested by *Li and Leighton* [1992], no significant improvement is found on the regressions of either viewing and solar zenith angles. In Figure 3, we have plotted the ratio between ρ_m and ϱ_c associated to the values of Figure 1. As one can see, the maximum variation of θ_0 over 60 days is about 20°, while the corresponding variation of the base curve of the ratio (associated to clear-sky conditions) is limited to about 6%.

3. Choice of Parameters

[10] It is worth pointing out that the time period, N, over which the percentile is computed cannot be too short;

Table 2. Number of Pixels for Each Earth Radiation Budget Experiment Geotype in the Clear-Sky Reduced Database

Geotype	Pixels	Fraction, %
Ocean	8,030	13
Vegetation	18,575	31
Desert	33,492	56

Table 3. Statistics (Bias, Standard Deviation, and Root-Mean-Square Deviation) on Absolute Errors of Clear-Sky Reflectances According to the RGP and ISCCP Algorithms for the Reduced Database

Geotype	RMIB GERB Processing[a]			ISCCP Processing[b]		
	Bias	Standard Deviation	Root-Mean-Square Deviation	Bias	Standard Deviation	Root-Mean-Square Deviation
Ocean	0.003	0.004	0.005	0.017	0.005	0.017
Vegetation	−0.012	0.011	0.016	−0.002	0.024	0.024
Desert	−0.017	0.016	0.023	−0.004	0.043	0.043

[a]RMIB GERB is Royal Meteorological Institute of Belgium Geostationary Earth Radiation Budget.
[b]ISCCP is International Satellite Cloud Climatology Project.

otherwise, the method reduces to a search for the minimum value of $\rho_m(d, t^\star)/\varrho_c(d, t^\star)$. This will therefore lead to an unacceptable sensitivity toward cloud shadows (characterized by an abrupt and sudden decrease of the measured reflectance) as previously mentioned. On the other hand, a too large time period could violate our assumption regarding the stability of vegetation. According to *Matthews and Rossow* [1987] some portions of the African tropical land area present persistent cloudiness over more than 30 days. This can lead to large errors in the retrieved clear-sky reflectances from algorithms using a base period of time lower than 60 days. The influence of the time period length on the computed visible clear-sky reflectance values is displayed in Figure 4. As we can see, the smoothness of the clear-sky curve increases with increasing N. This is a direct effect of our statistical approach. Moreover, our implicit assumption regarding the proportionality between the shortwave CERES and the visible clear-sky reflectance curves over a given time period is not necessarily valid for large N. Indeed, Figure 4 clearly indicates that as the value of N increases, the computed clear-sky visible reflectances tend to be underestimated. For all these reasons, setting N equal to 60 days appears to be a good compromise.

[11] In section 2, we chose 5% as the percentile value for our algorithm. As already mentioned, the measured signal can be seen as the clear-sky base curve plus a random additive noise representing the clouds contribution (positive) and the cloud shadows effect (negative). A too small threshold on the percentile value would lead to unacceptable sensitivity to shadow occurrences, while a too high value would result in the selection of a cloudy α value to compute the clear-sky reflectance. Thus fixing the threshold to 5% guarantees that we will successfully filter in our scheme up to three measurements associated to cloud shadows within 60 days, while requiring at least four clear-sky reflectances on the same time period. Qualitative tests have shown the spatial and temporal robustness of this value.

[12] Nevertheless, in section 4 these values will be implicitly validated. Note that the applicability of our

algorithm is not limited to ocean surfaces. Figure 5 illustrates its results over an ocean surface pixel.

4. Algorithm Performance

[13] In order to assess the improvement of our method with regards to region-based algorithms such as the one implemented in ISCCP, we have built a clear-sky pixels database by visually selecting cloud-free pixels. Owing to the exhaustive manual work this step requires, we only have selected 3 days with 1 month interval between each others, i.e., the firsts of August, September, and October 1998. Those clear-sky pixels were selected from 0800 to 1600 UTC on a 1 hour time step basis and in every surface geotype. For convenience, we have chosen to stratify them according to the simple ERBE surface classification (ocean, vegetation, and desert). Note that the day and hour samplings in this database does not decrease its generality because we are capturing during these three months the main temporal changes in the reflectance of vegetation coverage. However, to easily compare our results with ISCCP, we only considered pixels belonging to ISCCP time slots, i.e., 0900, 1200, and 1500 UTC (reduced database). Table 2 gives the population within each ERBE surface class. Finally, for each pixel of this database, we have computed its clear-sky reflectance as estimated by our algorithm with the fifth percentile and $N = 60$ days. The comparisons between these values and the real ones are shown in Tables 3 and 4.

[14] To directly compare our results with ISCCP, we have selected the associated MS-7 ISCCP Pixel Level Cloud Products with a native spatial resolution of 30 km [*Rossow et al.*, 1996]. From these data, we have converted the extracted composite (on 10 days) clear-sky radiances into reflectances using the absolute ISCCP calibration across all satellites participating in this project [*Brest et al.*, 1997]. Then, for every clear-sky pixel in our reduced database, we have taken the reflectance value associated to the nearest ISCCP data point. To cope for possible differences between

Table 4. Statistics (Bias, Standard Deviation, and Root-Mean-Square Deviation) on Relative Errors of Clear-Sky Reflectances According to the RGP and ISCCP Algorithms in Percent for the Reduced Database

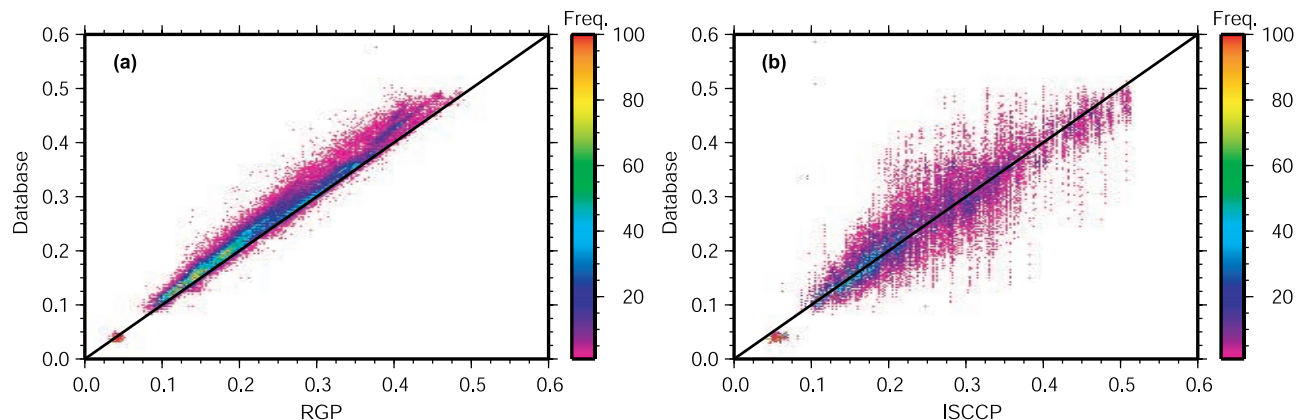| Geotype	RMIB GERB Processing			ISCCP Processing		
	Bias	Standard Deviation	Root-Mean-Square Deviation	Bias	Standard Deviation	Root-Mean-Square Deviation
Ocean	8.4	11.9	14.6	43.0	15.7	45.8
Vegetation	−7.0	5.7	9.0	0.4	14.1	14.1
Desert	−5.9	5.2	7.9	−0.2	16.2	16.2

Figure 6. (a) Estimated RGP and (b) ISCCP clear-sky reflectance versus clear-sky (reduced) database value.

ISCCP and EUMETSAT calibrations, we recomputed our cloud-free reflectance database according to ISCCP calibration. The comparisons of both results are given in the second part of Tables 3 and 4, and the associated scatterplots are given in Figure 6.

[15] As errors for each method have been computed according to a priori two different calibration schemes, we should first check and account for possible discrepancies between them before proceeding with any conclusion based on these results. It can be demonstrated by simply plotting (not shown) the measured reflectances for all (reduced) database clear-sky pixels that ISCCP and EUMETSAT calibration are almost identical. Indeed, such pairs of values have a correlation coefficient of 0.999885, while a linear best fit on these gives the law $\rho_E = 0.9927 \times \rho_I$. Thus the above errors in these tables can be directly compared. We notice that the overall error (root-mean-square deviation) of our method is significantly smaller than for ISCCP. This is also illustrated in Figure 6 where the ISCCP plot exhibits a larger scatter. Looking at the standard deviation of the relative error in Table 4, we notice that the scatter due to our method is about 10% lower than ISCCP for vegetation and desert (surface types associated with large reflectance values), while for ocean, which has usually a minimal response in the visible spectrum (≤ 0.05), it is about 4% lower.

[16] However, except for the ocean, where there seems to be some problem with ISCCP clear-sky algorithm, our scheme systematically has a larger bias than ISCCP. This could result from the three additional effects occurring and contributing to some extent to the signal: (1) variability due to changes in aerosol content, (2) variability induced by the discrete quantification of the detectors (8 bits for MS-7), and (3) variations due to the movement of the satellite which are compensated in the image registration process (interpolation) on a fixed geolocation grid. These three effects are clearly illustrated in Figure 4 before the 240th Julian day where all the previous days have cloud-free conditions, while the reflectance time series exhibits some random fluctuations around its mean clear-sky value. These perturbations can reach up to 10% of the mean value for desert pixels and other surfaces with high reflectance values such as vegetation. Investigating more closely the sign of the bias in Table 4, we notice that our method tends to underestimate the clear-sky values over land. This would suggest to increase the threshold above the fifth percentile over these surfaces.

[17] Moreover, our method was checked to perform well on other time slots. In Table 5, we have given the statistics on the relative error distribution between RGP clear-sky estimates and associated values of the complete database (including all daytime hours from 0800 to 1600 UTC). One can notice these values are nearly identical compared to the ones found in Table 4.

[18] However, our database is not adequate to estimate the optimal percentile and time period, N, for each major surface class due to the difficulty of selecting pixels where cloud shadows occur in their associated time series. It is primarly due to the fact that our clear-sky database was only built on three days of data. A possible future improvement of our method could be the estimation of such optimal parameters, but this step will need a clear-sky database covering a large temporal period (ideally 1 year).

5. Final Remarks and Perspectives

[19] The new statistical method we develop to determine the composite clear-sky reflectance images in the visible part of the spectrum uses a priori knowledge of angular variations of surfaces reflectance through the clear-sky CERES broadband ADMs. The strength of these models is that they have been built from experimental data around the world over a long period of time, accounting therefore for correct averaged spatiotemporal responses for each of their surface classes.

Table 5. Statistics (Bias, Standard Deviation, and Root-Mean-Square Deviation) on Relative Errors of Clear-Sky Reflectances According to the RGP Algorithm in Percent for the Complete Database

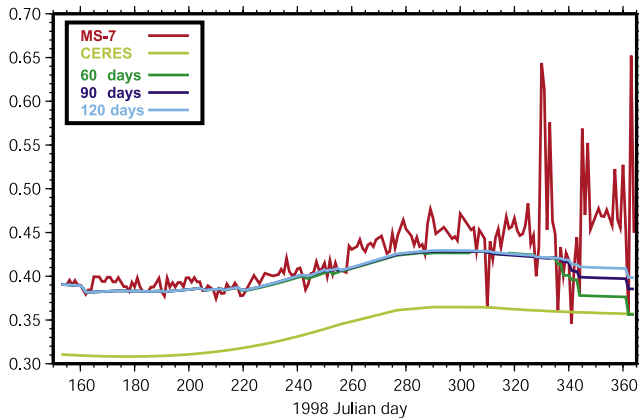| Geotype | RMIB GERB Processing | | | Population | |
	Bias	Standard Deviation	Root-Mean-Square Deviation	Pixels	Fraction, %
Ocean	8.7	11.8	14.7	18,855	10
Vegetation	−6.5	6.8	9.4	60,186	33
Desert	−5.9	5.5	8.0	106,494	57

Figure 7. Meteosat-7 visible reflectance time series, ρ_m, and its associated clear-sky broadband CERES reflectances, ϱ_c, according to the scene-viewing geometry variations from the 1200 UTC daily measurements over a bright desert pixel (28.13°N, 29.19°E) and our algorithm visible clear-sky predicted values ρ_{cs} for several N.

[20] Nevertheless, as illustrated in Figure 7, some limitations appear in the presence of high occurrence of cloud shadows within the considered period of time. As we see, the 60 day values are moved down due to several minima in the recorded radiance time series. A possible way to solve this weakness could rely on the determination of the optimal percentile and time period, N, for each surface geotype and according possibly to location. However, this requires further investigations through the building of an exhaustive spatial and temporal clear-sky pixels database. Another technique could be the use of a cloud shadows detection scheme such as the one given by *Simpson et al.* [2000] in order to discard the associated reflectance values in the percentile computation.

[21] Moreover, fresh snow covers because of their high visible reflectance responses (same order of magnitude as thick clouds) can lead to a misevaluation by our algorithm of the associated clear-sky values and the cloud properties retrievals. To remedy to this, a snow detection procedure is generally applied in the a posteriori cloud identification scheme, but this is beyond the scope of this paper.

[22] Finally, this method was shown to perform better than the ISCCP scheme on MS-7. This should also hold for other geostationary satellites having similar MS-7-like wide visible channels. Nevertheless, this technique should be applicable to both SEVIRI visible narrow bands (0.6 μm and 0.8 μm) by simply substituting in our method the CERES shortwave ADMs by the visible Polarization and Directionality of the Earth's Reflectances (POLDER) TOA ADMs as generated by *Loeb et al.* [2000]. This will be investigated when sufficient SEVIRI data will be available.

References

Brest, C. L., W. B. Rossow, and M. Roiter, Update of radiance calibration for ISCCP, *J. Atmos. Ocean. Technol.*, *14*, 1091–1109, 1997.

Govaerts, Y. M., A. Arriaga, and J. Schmetz, Operational vicarious calibration of the MSG/SEVIRI solar channels, *Adv. Space Res.*, *28*, 21–30, 2001.

Gruber, A., and J. S. Winston, Earth-atmosphere radiative heating based on NOAA scanning radiometer measurements, *Bull. Am. Meteorol. Soc.*, *59*, 1570–1573, 1978.

Li, Z., and H. G. Leighton, Narrowband to broadband conversion with spatially autocorrelated reflectance measurements, *J. Appl. Meteorol.*, *31*, 421–432, 1992.

Loeb, N. G., F. Parol, J. C. Buriez, and C. Vanbauce, Top-of-atmosphere albedo estimation from angular distribution models using scene identification from satellite cloud property retrievals, *J. Clim.*, *13*, 1269–1285, 2000.

Loeb, N. G., N. M. Smith, S. Kato, W. F. Miller, S. Gupta, P. Minnis, and B. A. Wielicki, Angular distribution models for top-of-atmosphere radiative flux estimation from the Clouds and the Earth's Radiant Energy System instrument on the Tropical Rainfall Measuring Mission Satellite. part I: Methodology, *J. Appl. Meteorol.*, *42*, 240–265, 2003.

Matthews, E., and W. B. Rossow, Regional and seasonal variations of surface reflectances from satellite observations at 0.6 μm, *J. Clim. Appl. Meteorol.*, *26*, 170–202, 1987.

Minnis, P., and E. F. Harrison, Diurnal variability of regional cloud and clear-sky radiative parameters derived from GOES data. part I: Analysis method, *J. Clim. Appl. Meteorol.*, *23*, 993–1011, 1984a.

Minnis, P., and E. F. Harrison, Diurnal variability of regional cloud and clear-sky radiative parameters derived from GOES data. part III: November 1978 radiative parameters, *J. Clim. Appl. Meteorol.*, *23*, 1032–1051, 1984b.

Rossow, W. B., and L. C. Garder, Cloud detection using satellite measurements of infrared and visible radiances for ISCCP, *J. Clim.*, *6*, 2341–2369, 1993.

Rossow, W. B., L.C. Garder, and A.A. Lacis, Global, seasonal cloud variations from satellite radiance measurements. part I: Sensitivity of analysis, *J. Clim.*, *2*, 419–458, 1989.

Rossow, W. B., A. W. Walker, D. E. Beuschel, and M. D. Roiter, International Satellite Cloud Climatology Project (ISCCP) documentation of new cloud datasets, *Rep. WMO/TD–737*, 115 pp., World Meteorol. Organ., Geneva, Switzerland, 1996.

Simpson, J. J., J. R. Stitt, and Z. Jin, Cloud shadow detection under arbitrary viewing and illumination conditions, *IEEE Trans. Geosci. Remote Sens.*, *38*, 972–976, 2000.

Stubenrauch, C. J., V. Briand, and W. B. Rossow, The role of clear-sky identification in the study of cloud radiative effects: Combined analysis from ISCCP and the scanner of radiation budget, *J. Appl. Meteorol.*, *41*, 396–412, 2002.

Suttles, J. T., R. N. Green, P. Minnis, G. L. Smith, W. F. Staylor, B. A. Wielicki, I. J. Walker, D. F. Young, V. R. Taylor, and L. L. Stowe, Angular radiation models for the Earth-atmosphere system, in *Shortwave Radiation*, vol. I, *NASA Ref. Publ., RP-1184*, 147 pp., 1988.

Taylor, V. R., and L. L. Stowe, Reflectance characteristics of uniform Earth and cloud surfaces derived from Nimbus 7 ERB, *J. Geophys. Res.*, *89*, 4987–4996, 1984.

———————————

C. Bertrand, N. Clerbaux, S. Dewitte, L. Gonzalez, and A. Ipe, Section Remote Sensing from Space, Department of Observations, Royal Meteorological Institute of Belgium (RMIB), Avenue Circulaire 3, B-1180 Brussels, Belgium. (Alessandro.Ipe@oma.be)